

Article

Core/Shell Structure of Mesoporous Carbon Spheres and g-C₃N₄ for Acid Red 18 Decolorization

Martyna Baca, Małgorzata Aleksandrak, Ewa Mijowska , Ryszard J. Kaleńczuk and Beata Zielińska * 

West Pomeranian University of Technology, Szczecin, Faculty of Chemical Technology and Engineering, Nanomaterials Physicochemistry Department, Piastow Ave. 45, 70-311 Szczecin, Poland; martyna.baca@zut.edu.pl (M.B.); Malgorzata.Aleksandrak@zut.edu.pl (M.A.); emijowska@zut.edu.pl (E.M.); rk@zut.edu.pl (R.J.K.)

* Correspondence: bzielinska@zut.edu.pl

Received: 30 September 2019; Accepted: 27 November 2019; Published: 30 November 2019



Abstract: Spherical photocatalyst based on ordered mesoporous carbon and graphitic carbon nitride with core/shell structure (CS/GCN) was successfully synthesized via facile electrostatic self-assembly strategy. The photocatalytic properties of the hybrid were evaluated by the decomposition of Acid Red 18 under simulated solar light irradiation in comparison to the bulk graphitic carbon nitride (GCN). The results clearly revealed that coupling of carbon nitride with mesoporous carbon allows the catalyst to form with superior photocatalytic performance. The photoactivity of CS/GCN was over nine times higher than that of pristine GCN. Introducing mesoporous carbon into GCN induced higher surface area of the heterojunction and also facilitated the contact surface between the two phases. The synergistic effect between those two components enhanced the visible light-harvesting efficiency and improved photoinduced charge carrier generation, and consequently their proper separation. The electrochemical behavior of the obtained composite was also evaluated by electrochemical impedance, transient photocurrent response and linear sweep potentiometry measurements. The results confirmed that transport and separation of charge carriers in the hybrid was enhanced in comparison to the reference bulk graphitic carbon nitride. Detailed electrochemical, photoluminescence and radical scavenger tests enabled determination of the possible mechanism of photocatalytic process. This work presents new insights to design a core/shell hybrid through the simple preparation process, which can be successfully used as an efficient photocatalyst for the treatment of wastewater containing dyes under solar light irradiation.

Keywords: graphitic carbon nitride; mesoporous carbon; core/shell structures; dye removal; photocatalysis

1. Introduction

Recently, graphitic carbon nitride (g-C₃N₄, GCN) has received huge scientific interest due to its many advantages, including easy preparation, non-toxicity, high chemical and thermal stability, and moderate band gap leading to good visible-light response [1–5]. Thus, GCN is considered as a promising multifunctional catalyst for many processes such as photocatalytic decomposition of organic and inorganic pollutants, photocatalytic H₂ and O₂ evolution, CO₂ reduction and other energy conversion processes [4,6]. However, in the case of photocatalytic processes, three main shortcomings of the bulk GCN seriously limit its wide practical application: (i) ineffective utilization of vis-light via absorption of narrow part of the solar energy (>460 nm), (ii) fast recombination of photoinduced carriers, and (iii) quite small surface area [7–9]. The first and second disadvantage can be manipulated by coupling GCN with narrow band gap semiconductors that possess proper energy levels. In order to

increase the surface area, the porosity in the structure of GCN can be additionally induced. Mesoporous photocatalysts received considerable research interest because they contain a special pore network, which facilitates the diffusion of the reactants and products. Moreover, the large surface area offers more active sites. Therefore, for an economical utilization of GCN, the researchers should strive to find the way for enhancing its photocatalytic properties [10,11].

Up to now, different strategies, including introducing foreign elements, designing nanoporous structures, texturization, supramolecular assembly and creating effective heterojunctions, have been developed to enhance the photoactivity of GCN [12]. A large number of studies have confirmed that building a heterojunction system is an effective method to improve the separation efficiency of the photogenerated electrons and holes which dramatically improves the photocatalytic performance [13]. To form an efficient heterojunction, GCN has been coupled with other semiconductors such as TiO₂, Ag₂O, ZnO, CdS, SnO₂, WO₃, Cu₂O, Bi₂S₃, AgI, AgBr, MoS₂, Ag₃PO₄, BiOI, etc. [12,14–21]. Unfortunately, the particles (often in the agglomerated form) were usually loaded randomly on the GCN sheets in composites causing low conjunction of GCN with a semiconductor which consequently limited charge transfer and separation efficiency. Therefore, it is crucial to design a new class of hybrid catalysts with a high effective area of the heterojunction because the larger area of heterojunction will result in higher separation efficiency of the photoinduced carriers. It has been revealed that formation of core/shell nanostructures is considered as a promising method to increase the contact surface between the two phases, and as a consequence, to enhance the visible light-harvesting efficiency and photocatalytic activity of nanostructured catalysts.

There are some reports on the synthesis and physicochemical characterization of core/shell structures based on GCN and different semiconductors. Some metal semiconductors such as ZnO [22], BiVO₄ [23], SnO₂ [24], MoS₂ [25] and TiO₂ [26] have been investigated as cores for GCN. It has been stated that these core/shell catalysts exhibit high photostability and higher photocatalytic activity than that of the pristine core materials and GCN. Y. Yao et al. [27] synthesized CuFe₂O₃/GCN core/shell hybrids for vis-light photocatalytic decomposition of Orange II. It was found that CuFe₂O₄/GCN with mass ratio of 2:1 exhibited superior activity as compared to a single component of CuFe₂O₄ or GCN. This is due to the elevation of the separation efficiency of photogenerated electron–hole pairs, resulted from the heterojunction between GCN and CuFe₂O₄. Moreover, it has been proven that core/shell hybrids exhibit higher activity than that of the mixture of GCN and CuFe₂O₄, where CuFe₂O₄ was deposited on GCN. More importantly, the CuFe₂O₄/GCN could efficiently degrade various organic pollutants under vis-light irradiation and exhibit an excellent photocatalytic performance after many cycles without considerable activity loss. Furthermore, researchers have indicated a bright horizon of increasing graphitic carbon nitride photocatalytic ability through hybridization with carbon sources. Liu et. al. [28] synthesized carbon spheres with controllable size (200–500 nm), which further were deposited onto graphitic carbon nitride sheets via hydrothermal process. It was found that all composites displayed enhanced photocatalytic performance under visible light in degradation of water contaminants such as methylene blue and antibiotic sulfachloropyridazine. Moreover, it was confirmed that carbon spheres had the ability to capture the electrons, thus causing better charge carrier separation. Similarly, g-C₃N₄-encapsulating carbon spheres (CS/g-C₃N₄) were produced in facile polymerization of melamine approach [29]. CS/g-C₃N₄ displayed nearly five-times higher photocatalytic hydrogen generation rate in comparison to the pristine graphitic carbon nitride. Despite very promising results, the coupling of graphitic carbon nitride with carbon spheres, especially mesoporous carbon spheres, is still the least investigated field.

In this study, the spherical core/shell hybrid (CS/GCN) was prepared via facile chemical route in which the bulk GCN was protonated using strong oxidant and further deposited on the surface of mesoporous carbon spheres. The photocatalytic performance of the obtained hybrid (in comparison to the bulk GCN) was evaluated by Acid Red 18 decolorization process under simulated solar light irradiation. The electrochemical properties of the obtained samples were also studied. The mechanism of the photoinduced electron–hole pairs distribution between the individual components of the hybrid

and the influence of this effect on the AR18 decomposition process have also been discussed in great detail.

2. Results and Discussion

The atomic force microscope was employed to study the GCN topography (Figure 1). The thickness of the bulk GCN flakes was in the range of 22–55 nm with the lateral size of 1–4 μm . The theoretical thickness of g- C_3N_4 monolayer is estimated at ~ 0.325 nm [30], which means that the obtained GCN was composed of about 90 to 170 layers. This result is in full agreement with the literature [30–32].

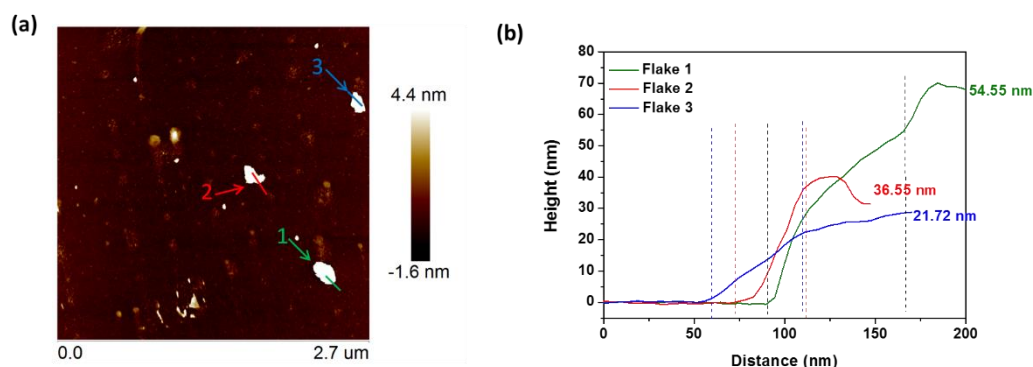


Figure 1. Atomic force microscopy (AFM) images and height profiles of graphitic carbon nitride (GCN).

In order to confirm that formation of CS/GCN hybrid occurs through the spontaneous self-assembly process between carbon core and carbon nitride shell, the zeta potential of CS, GCN, pGCN (GCN after acid treatment) and CS/GCN was measured (Figure 2). The protonation process modified the carbon nitride charge surface from negative -20.4 mV (GCN) to positive $+49.1$ mV (pGCN). Furthermore, the carbon spheres surface was enriched in oxygen containing functional groups, thus CS exhibited negative ζ potential value (-24.7 mV). Deposition of carbon nitride onto carbon spheres surface modified zeta potential of composite to positive ($+32.9$ mV). These results confirmed that the stable hybrids were formed through various interactions such as π - π stacking and electrostatic interactions [33,34].

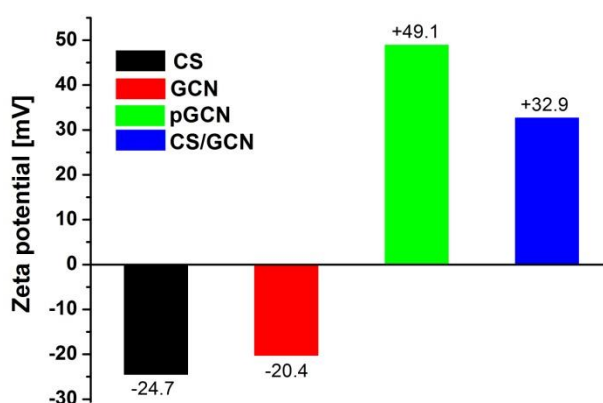


Figure 2. Zeta potential of the carbon spheres (CS), GCN, protonated graphitic carbon nitride (pGCN) and CS/GCN.

Figure 3 shows TEM images of GCN, CS and CS/GCN samples. The graphitic carbon nitride exhibited few-layered structure (see Figure 3a). The carbon spheres (Figure 3b,c) demonstrated smooth surface with uniform spherical shape morphology and diameter in the range of 550–650 nm. The surface of CS/GCN is irregular. Those irregularities were assigned to the graphitic carbon nitride (Figure 3d–f). No impurities were observed in the sample, thus the CS/GCN undoubtedly consists

of carbon and tightly anchored GCN on the surface. To confirm this, the elemental compositions of CS/GCN was examined by Energy-dispersive X-ray spectroscopy (EDS) measurements (Figure 4). EDS spectrum displays that carbon, nitrogen and oxygen are the only elements in the CS/GCN. Moreover, the elements are uniformly distributed in the sample.

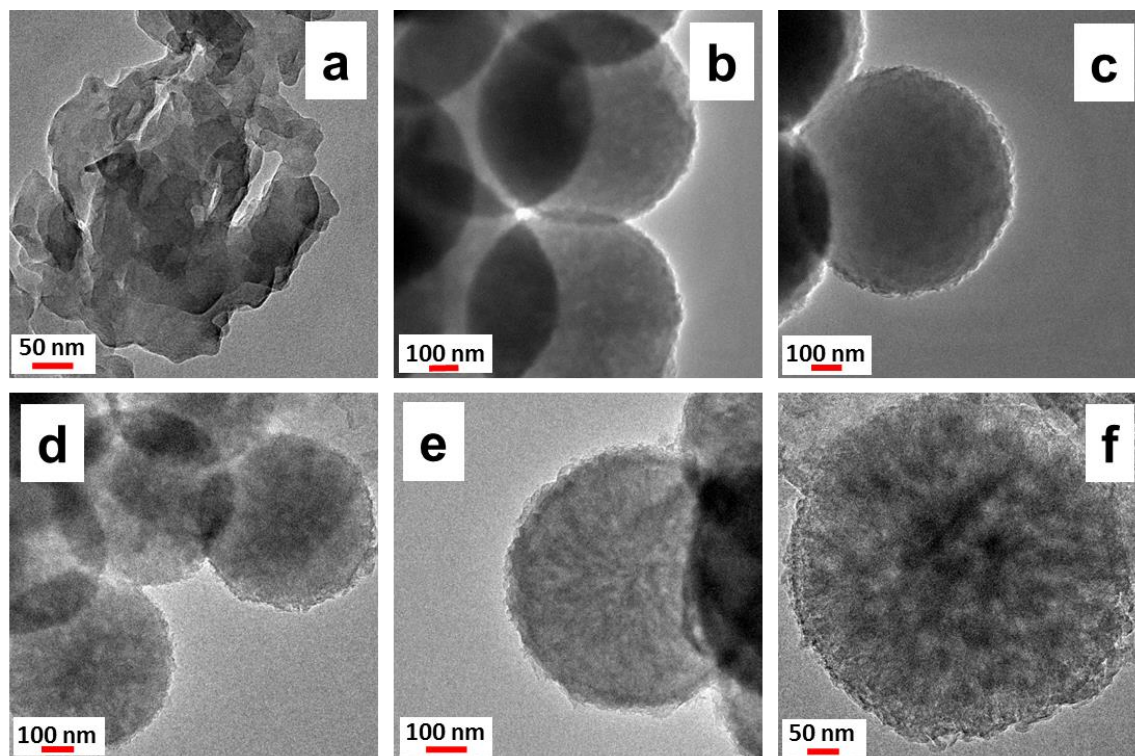


Figure 3. TEM images of GCN (a), CS (b,c) and CS/GCN (d–f).

To further evaluate the structural properties of the obtained materials, the specific surface area and pore size distribution were analyzed. The nitrogen adsorption–desorption isotherms at 77 K and pore size distribution, measured according to density functional theory (DFT method), are shown in Figure 5. Additionally, Table 1 contains data on specific surface area of the samples and their total pore volume. In accordance with IUPAC classification, all samples exhibited IV type isotherm with final saturation plateau of specific length (or merely inflexion point) and typical hysteresis loop caused by the capillary condensation, characteristic for the mesoporous materials [35–37]. The hysteresis loop for CS and CS/GCN samples is similar to H2 (a) type hysteresis described by steep desorption branch assigned to the network effects such as pore-blocking/percolation in a narrow pore necks widths or evaporation via cavitation [36–38]. The main characteristic features of an H2 hysteresis loop are ink bottle pores and closed wedge pores [37,39]. Unmodified carbon spheres possess well-developed Brunauer–Emmett–Teller (BET) specific surface area of 290.34 m²/g. The specific surface area of CS/GCN (92.09 m²/g) was lower than CS, but still about five times higher than bulk GCN (17.82 m²/g). The pore size distribution (Figure 5b) indicates the presence of mesopores (2–7 nm) in all samples. The pore volume of CS/GCN increased to 0.2126 cm³/g from 0.1292 cm³/g (bulk GCN). Therefore, the conjugation of carbon spheres and graphitic carbon nitride resulted in the formation of unique composite with significantly improved textural properties.

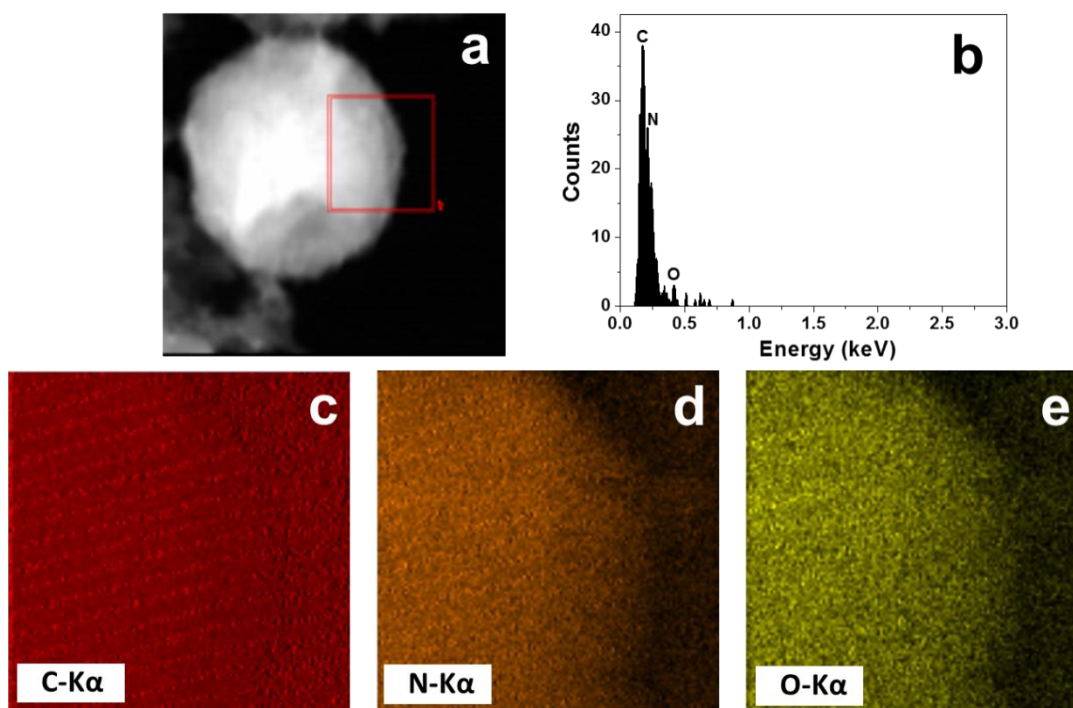


Figure 4. Scanning transmission electron microscopy (STEM) images (red square shows the scanned area) (a), Energy-dispersive X-ray spectroscopy (EDS) spectrum (b) and EDS elemental mapping of CS/GCN (c,d).

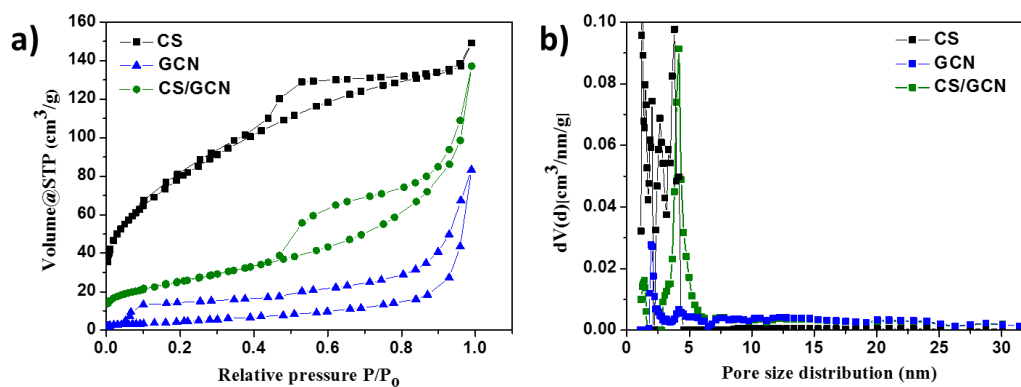


Figure 5. N₂ adsorption-desorption isotherms (a) and pore size distribution (b) for CS, GCN and CS/GCN.

Table 1. Characteristic of CS, GCN and CS/GCN.

Sample	Brunauer–Emmett–Teller (BET) Surface Area (m ² /g)	Total Pore Volume (cm ³ /g)	Band Gap Energy (eV)
CS	290.34	0.23	-
GCN	17.82	0.13	2.72
CS/GCN	92.09	0.21	2.96

XRD patterns of the synthesized samples are illustrated in Figure 6a. The pattern of CS shows two broad and low intensity peaks at 2θ value of 24° and 43° corresponding to the (002) and (100) planes of graphitic carbons [40]. The characteristic peaks associated to graphitic carbon nitride are identified in GCN and CS/GCN. The GCN exhibits two reflections at 2θ value of 27.4° and 13.1° . Those peaks can be indexed to the (002) and (100) planes which are related to the inter-planar stacking of aromatic

systems and in-plane regular arrangement of tri-s-triazine units, respectively [41,42]. For CS/GCN, the main (002) peak position is shifted of 0.05° toward higher angles compared to the bulk GCN. It is due to the expansion of the interlayer stacking distance of the layers in GCN, and this confirms that the bulk GCN was exfoliated after acid treatment [33,43]. Moreover, in CS/GCN the diffraction peaks at 24° and 43° , attributed to carbon, are also detected.

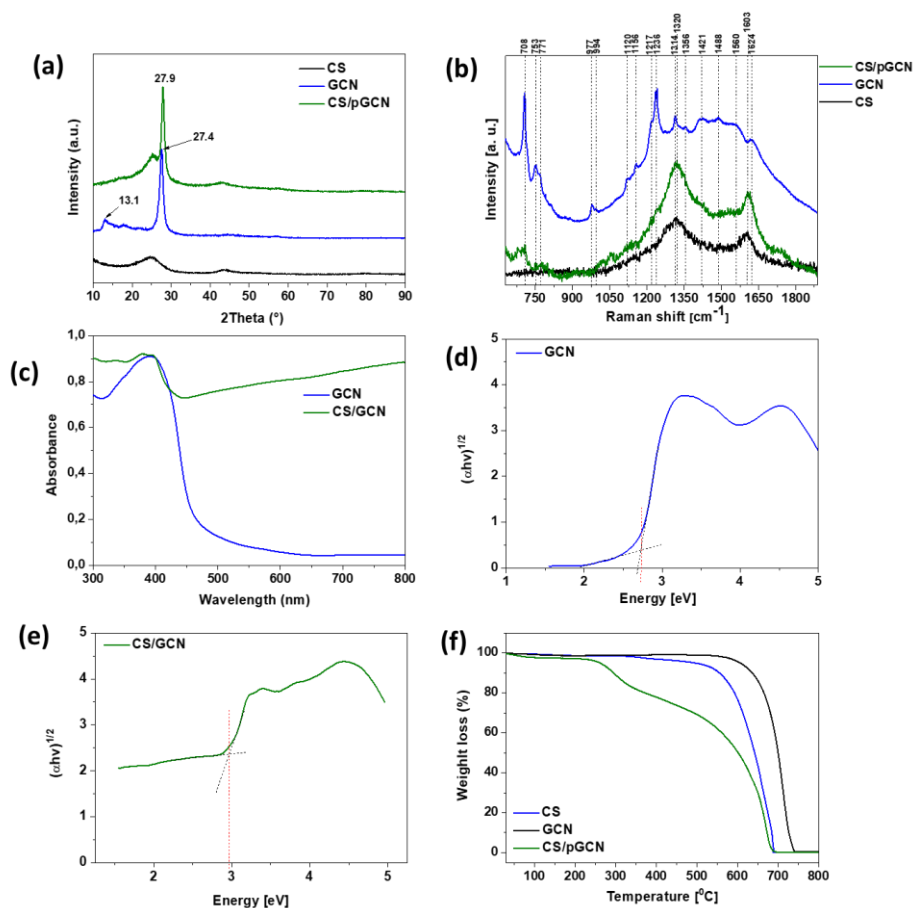


Figure 6. (a) XRD patterns, (b) Raman spectra, (c) UV/Vis absorption spectra, (d,e) Tauc plots and (f) TGA profiles of CS, GCN and CS/GCN.

Figure 6b depicts the Raman spectra of CS, GCN, and CS/GCN. The Raman responses undoubtedly confirm efficient synthesis of the hybrid material based on CS and GCN. The existence of the characteristic bands for GCN are shown, both in bulk material and in the composite. According to the literature [44–46], the several bands observed in the range of $700\text{--}1630\text{ cm}^{-1}$ are attributed to the bulk GCN. Moreover, the vibration modes at $753, 977, 1120, 1156, 1236$ and 1314 cm^{-1} are assigned to the stretching vibration of aromatic C–N heterocycle characteristic to melem. Furthermore, the peaks at $700\text{--}1000\text{ cm}^{-1}$ region were ascribed to the various types of ring breathing modes of s-triazine [28,47]. Moreover, the Raman response of the bulk GCN shows D (1356 cm^{-1}) and G (1560 cm^{-1}) bands which confirmed the presence of carbon structure in the sample [48,49]. The D (1320 cm^{-1}) and G bands (1603 cm^{-1}) observed in CS are associated to: (i) sp^3 defects derived from the disorder in sp^2 bonding and (ii) in-plane vibrational mode involving sp^2 -hybridized C–C bonds attributed to graphitic structure of the carbon spheres, respectively. For CS/GCN, the weak modes of graphitic carbon nitride ($708, 753, 771\text{ cm}^{-1}$) and strong D and G bands of CS are observed. The intensity ratio of D/G of the pristine CS was 1.36, whereas for CS/GCN it increased to 1.41. It indicates that introduction of carbon nitride to the hybrid caused formation of more defects in the carbon framework [50]. This result was consistent

with XRD analysis and confirmed that the fabricated CS/GCN were composed of carbon and graphitic carbon nitride.

The UV/Vis absorption spectra of the synthesized samples (GCN and CS/GCN) are displayed in Figure 6c. The band gap energy of GCN and CS/GCN was determined using Tauc plots with linear extrapolation as shown in Figure 6d and e, respectively. The estimated band gap of the reference GCN was 2.72 eV. After the deposition of graphitic carbon nitride on mesoporous carbon spheres (CS/GCN) increasing of band gap value to 2.96 eV was observed. It is due to chemical exfoliation of GCN occurring in the first stage of CS/GCN synthesis (HNO_3 treatment). This result is consistent with literature [30]. Moreover, the absorption intensity of CS/GCN under visible light increased.

Thermogravimetric (TG) analysis was performed to reveal the thermal behavior of the investigated materials and the analysis is shown in Figure 6d. In the bulk GCN, a weight loss at 600–750 °C was due to the direct thermal decomposition and complete vaporization of GCN itself, which confirms its high thermal stability and nonvolatile properties. The total decomposition of GCN occurred at approximately 750 °C. No residues were collected. Carbon spheres began to decompose at ~340 °C. At this temperate amorphous carbon was burnt. However, the steep decline can be observed at 525 °C and the complete combustion of the sample occurred at 700 °C. The ash content was 0 wt%, indicating high purity of CS. The thermal stability of CS/GCN decreased in comparison to the pristine GCN and CS. Moreover, the lower thermal stability of CS/GCN can be ascribed to the increased defects associated with the deposition of GCN onto CS surface which is in agreement with Raman study [51–54].

The X-ray photoelectron spectroscopy enabled to investigate the chemical states in composite and reference material (Figure 7). Three peaks in the fitted C1s spectrum of CS/GCN with their binding energies at around 284.6, 286.1 and 287.9 eV may be assigned to the presence of sp^2 C–C bonds, C– NH_x ($x = 1, 2$) species and C–N–C, respectively. The deconvolution of N1s spectrum of composite reveals three peaks with binding energy at 398.3, 399.6 and 400.8 eV related to sp^2 -hybridized nitrogen (C–N–C), sp^3 -tertiary nitrogen (N–[C]3) and NH_x groups, which are typical to the heptazine units of GCN.

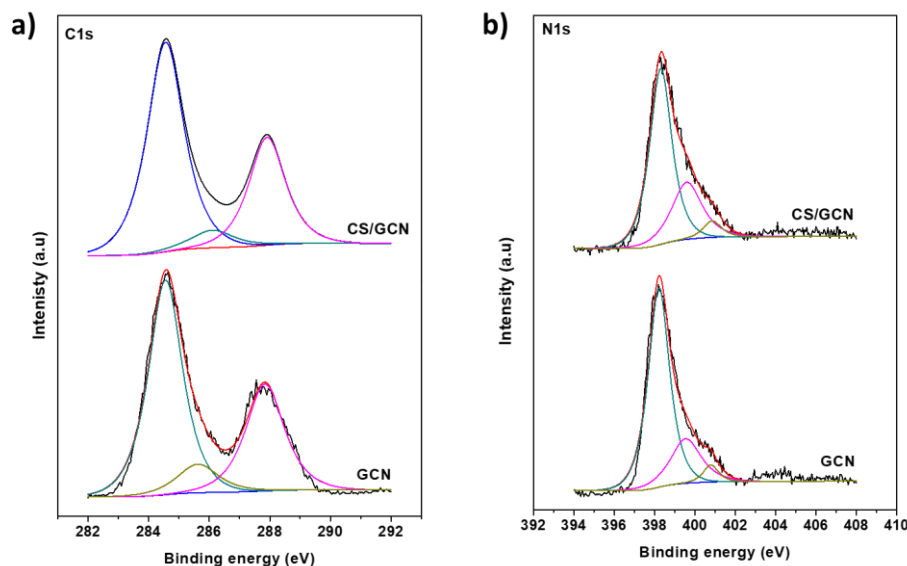


Figure 7. The deconvoluted C1s spectra and (a) N1s spectra (b) of GCN and CS/GCN recorded by high resolution XPS characterization.

The photocatalytic activity of the obtained samples was determined in the reaction of AR18 decomposition under simulated solar light irradiation at room temperature. As shown in Figure 8a, in the blank test (i.e., without addition of the photocatalysts), AR18 exhibited negligible self-decomposition, revealing great stability of the dye in the process. It is known that various processes can be involved in dye solution decolorization [55,56], therefore adsorption of AR18 on CS/GCN in darkness was also

performed (Figure 8c). The results revealed that adsorption equilibrium for CS/GCN was achieved after 1 h. Moreover, the lowest adsorption capacity was demonstrated by the bulk GCN (~3%). The enhanced adsorption performance of CS/GCN (~15%) is attributed to the higher surface area (~92 m²/g) and reduced particles agglomeration in respect to GCN. The photoactivity of GCN was rather low. Only 30% of AR18 removal after 12 h of irradiation was detected. The CS/GCN exhibited higher photocatalytic activity in the studied reaction: The degree of AR18 decomposition was over 96%. Figure 8b shows that the photocatalytic degradation of AR18 follows the pseudo first-order kinetics model, thus the dye removal rate constant k (min⁻¹) was calculated by the following equation:

$$\ln(C/C_0) = -kt$$

Where C_0 is the initial concentration of AR18 (10 mg/dm³), C is concentration at proper reaction time and t is the irradiation time. The calculated rate constants are $0.47 \times 10^{-3} \text{ min}^{-1}$ ($R^2 = 0.9935$) and $0.4 \times 10^{-2} \text{ min}^{-1}$ ($R^2 = 0.9889$) for GCN and CS/GCN, respectively. The rate constant of CS/GCN is over nine times higher than GCN [33,34,57–60]. Moreover, the comparative study with use of protonated graphitic carbon nitride (pGCN) as photocatalyst for AR18 decomposition has been performed (data not shown here). The photocatalytic activity of pGCN is ~3.5 times lower in respect to CS/GCN.

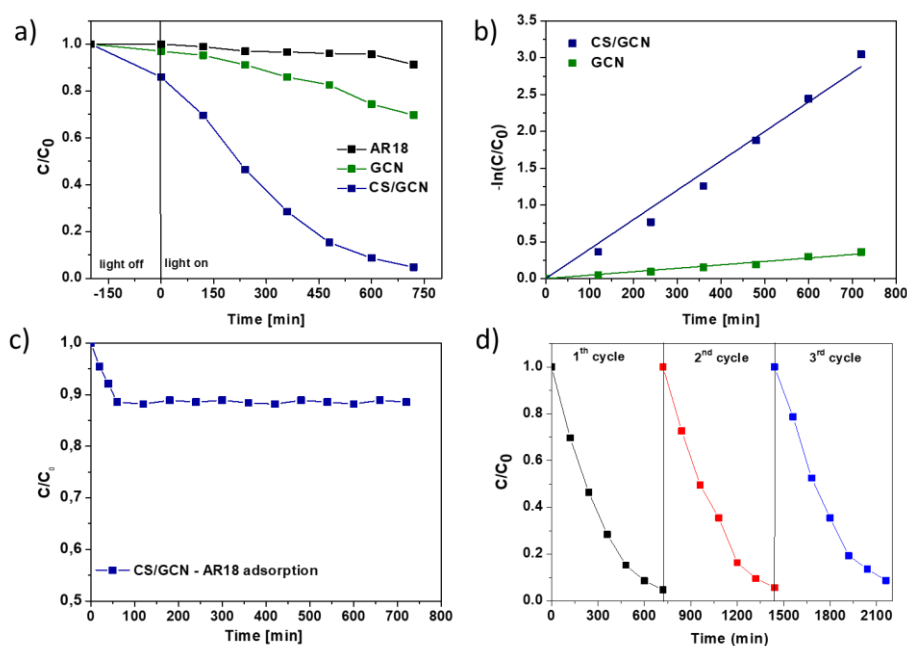


Figure 8. The photocatalytic degradation (a) and kinetic fit for the degradation of AR18 over GCN and CS/GCN (b); AR18 adsorption on CS/GCN in darkness (c); recyclability of CS/GCN for the decomposition of AR18 (d).

To assess long-term utility and durability of the photocatalyst, the CS/GCN was reused three times in the photocatalytic degradation process. As shown in Figure 8d the hybrid maintains its superior photocatalytic efficiency after three recycles.

To study the charge transfer at the semiconductor/electrolyte interface, EIS spectroscopy was measured in darkness and spectra are presented in Figure 9a. The inset in Figure 9a presents an equivalent model, where R_2 is charge transfer resistance (R_{ct}). According to the model, the R_{ct} decreased in the following direction: GCN > CS/GCN > CS, indicating improved interfacial charge transfer after graphitic carbon nitride hybridization with carbon spheres.

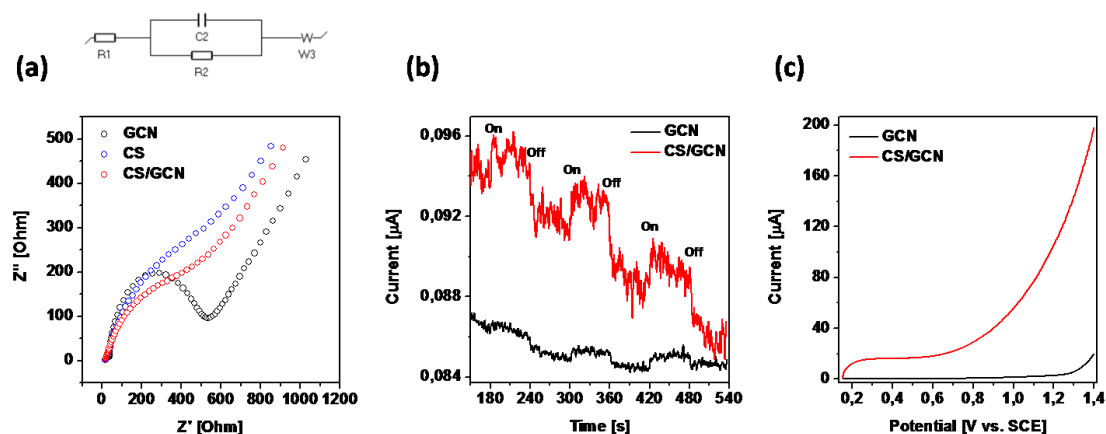


Figure 9. (a) EIS spectra with equivalent model, (b) transient photocurrent response, and (c) LSV of GCN, CS and CS/gCN. EIS was performed in darkness, transient photocurrent response and LSV measurements were conducted with 400–700 nm light irradiation.

To study the optical properties of GCN and CS/GCN, the photoluminescence (PL) spectra were collected. The PL analysis enables to reveal the main determinants of the photocatalytic reaction such as charge carrier recombination, transfer and separation. Figure 10a shows that both samples exhibit emission peak in vis light region. For CS/GCN the PL intensity is almost four times lower in comparison to the unmodified material, which is in good agreement with the photocatalytic data. The results show that the interfacial interaction in the CS/GCN composite heterojunction favors photo-induced charge carriers separation, improving electron shuttling from GCN to CS and suppressing the electron–hole recombination.

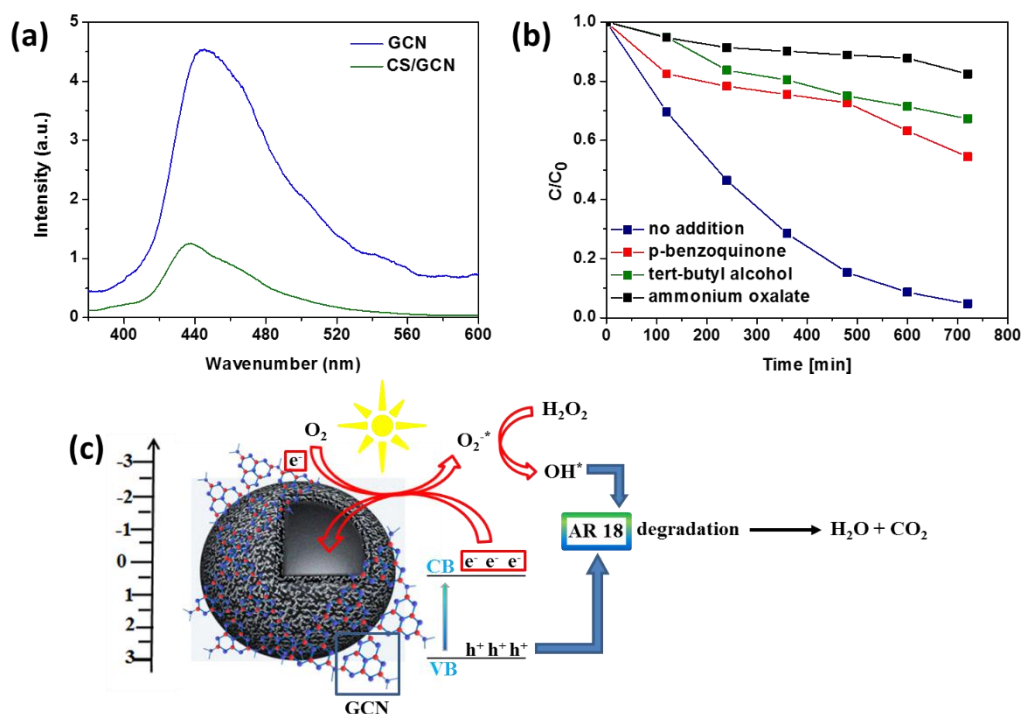


Figure 10. (a) PL spectra of GCN and CS/GCN, (b) effect of scavenger additive on the photocatalytic decomposition of AR18 over CS/GCN, and (c) schematic illustration of the mechanism of photocatalytic decomposition of AR18 over CS/GCN.

Transient photocurrent response and LSV technique (Figure 9b,c) were used to further investigate the photogenerated charge carrier transport and separation behavior. Both techniques revealed the enhanced photocurrent response after graphitic carbon nitride incorporation into carbon spheres. This confirms improved transport and separation behavior of the nanocomposite in comparison to the bulk graphitic carbon nitride, which is in good agreement of PL spectroscopy. Despite the suitable band alignment of the hybrid components, it can be also related to the proper light harvesting owing to sp^2 carbon clusters and enhanced active surface area.

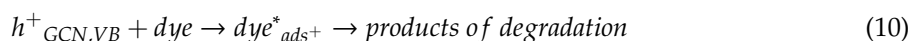
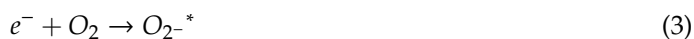
In order to propose the possible mechanism of the photocatalytic AR18 degradation, the reactive oxidative species (ROS), responsible for dye removing, should be assessed. Three scavengers such as tert-butyl alcohol (t-BuOH), ammonium oxalate ($C_2H_8N_2O_4$) and p-benzoquinone ($C_6H_4O_2$) were used as scavengers for hydroxyl radicals ($\bullet OH$), holes (h^+) and superoxide radicals ($\bullet O_2^-$) in decolorization of AR18, respectively. The photocatalytic decomposition of AR18 over CS/GCN and in the presence of the above-mentioned scavengers is presented in Figure 10b. The proposed mechanism is illustrated in Figure 10c. Moreover, the possible mechanistic pathways for the degradation of AR18 over CS/GCN are described in Equations(1)–(10).

The decomposition rate of AR18 decreased from 96% (no scavengers) to 46, 33 and 18% with the addition of $C_6H_4O_2$, t-BuOH and $C_2H_8N_2O_4$, respectively. It strongly indicated that all h^+ , $\bullet OH$ and $\bullet O_2^-$ were the active species involved in the photodegradation process. The degradation of AR18 was delayed most significantly in the presence of the holes scavenger (ammonium oxalate) which points out that the oxidation reactions occurred mainly via this reactive oxidative species (10).

The results revealed that carbon spheres play the key role in the enhancement of the photoactivity of GCN under simulated solar light irradiation. This is due to the synergistic effect between GCN shell and mesoporous carbon core. The carbon core serves as an acceptor of photogenerated electrons in conduction band (CB) of GCN, thereby facilitating the separation of photoinduced charge carriers. This efficient separation of electron–hole pairs inhibits the rapid recombination of charge carriers and extends the charge lifetime, leading to higher activity of CS/GCN. The photogenerated electrons after transfer to the carbon core are involved in the formation of $\bullet OH$ and $\bullet O_2^-$ radicals. Additionally, sp^2 carbon bonding also possesses high affinity to the incident light absorption serving as the support for the efficient dye degradation. The photons are absorbed through GCN under visible light irradiation, causing excitation of electrons and their transfer from valence band (VB) to conduction band (CB) (1). The holes are generated simultaneously in the VB. The ECB of GCN is more negative than $O_2/\bullet O_2^-$ potential (ca. -0.33 eV). Therefore, the electrons may react with oxygen adsorbed on the catalyst surface during the transfer to the carbon core forming $\bullet O_2^-$ radicals (2, 3). The holes in VB of GCN are not able to react with OH^- to yield $\bullet OH$ due to lower potential than $+1.99$ eV ($E_0(OH^-/\bullet OH) = +1.99$ eV/vs. NHE). However, $\bullet OH$ can be produced in various independent reactions, namely $\bullet O_2^-$ radicals could react with H_2O_2 to form $\bullet OH$, OH^- and O_2 (5). Peroxide radicals, ($HO_2\bullet$) formed through the reaction between $\bullet O_2^-$ and H^+ (6), could transform into hydrogen peroxide (H_2O_2) (7). Next, H_2O_2 could decompose into $\bullet OH$ after photon absorption from Vis region (8). Thereby, the radicals produced in the above described processes are responsible for the dye degradation [33,34,59,61].

Moreover, another mechanism of AR18 decomposition is also possible. For dyes showing absorption in the visible light range, the ability of the dye excitation itself should also be considered. This phenomenon is known as dye-sensitization, in which electrons of dye are excited by visible light absorption (11). The excited electrons (12) can be further transferred from the LUMO of dyes to the conduction band of GCN in CS/GCN composite (13). In this process cationic radicals and active electrons are formed. They promote O_2 reduction and formation of radical oxygen species (14). Moreover, cationic radicals can undergo further reactions resulting in dye decomposition (15) [62,63]. In order to prove that dye-sensitization is not a main mechanism of photocatalytic AR18 degradation, the reaction of photocatalytic decomposition of melamine, which shows absorption in UV light range, over CS/GCN under simulated solar light irradiation was also conducted (Supplementary Materials,

Figure S1). The results clearly revealed that CS/GCN exhibited photoactivity in the reaction of melamine decomposition. The melamine removal degree was over 99 % after 16 h of light irradiation.



3. Materials and Methods

3.1. Chemicals and Materials

Chemicals were purchased from Sigma Aldrich (melamine, Tetraethyl orthosilicate TEOS $\geq 99.0\%$ (GC), Hexadecyltrimethylammonium bromide CTAB $\geq 98\%$) or Chempur (nitric acid 65%, ammonia solution 25%) and used as received.

3.1.1. Preparation of Graphitic Carbon Nitride (GCN)

The bulk GCN was synthesized via thermal polycondensation of melamine (5 g) in a muffle furnace at the temperature of 550 °C for 2 h with a heating rate of 2 °C/min in air atmosphere. Then, the furnace was cooled down to room temperature and the obtained yellow product was collected and grounded into the powder. The yield of GCN synthesis was ~35%.

3.1.2. Preparation of Mesoporous Carbon Spheres (CS)

The mesoporous carbon spheres were prepared via chemical vapor deposition (CVD) method using mesoporous silica spheres (mSiO₂_CTAB) as template. mSiO₂_CTAB were synthesized via sol-gel reaction. Briefly, 60 mL of C₂H₅OH (99.8 %), 1.1 mL of NH₄OH (25 %) and 300 mg of CTAB were sonicated for 0.5 h and further mixed for another 0.5 h. Then 0.4 mL of TEOS was added dropwise to the solution and the mixture was stirred at room temperature for 12 h. Finally, the obtained silica spheres were centrifuged, washed with ethanol and distilled water and dried at 80 °C for 24 h. In a typical CS synthesis, the as-prepared SiO₂_CTAB template was placed in the alumina boat and introduced into the center of a horizontal quartz tube in the horizontal furnace. The furnace was heated under flowing argon (100 sccm) up to 800 °C. When the temperature was reached, ethylene was introduced with a flow rate of 30 cm³/min. CVD reaction time was 4 h. Afterwards, the furnace was cooled down

to room temperature in Ar. Finally, the obtained sample was treated with HF to remove the silica template, washed with distilled water and ethanol and dried at 80 °C for 24 h.

3.1.3. Preparation of CS/GCN Core/Shell Hybrid

First, the mixture of bulk GCN (1 g) and HNO₃ (60 mL, 65 wt %) was placed in a flask fitted with a reflux condenser and refluxed at 70 °C for 3 h. After that, 100 mg of CS was added into the above suspension and refluxed for additional 2 h. The solid product was washed several times with distilled water and heated at 250 °C for 2 h and the CS/GCN core/shell material was obtained. The schematic illustration of CS/GCN preparation is presented in Figure 11.

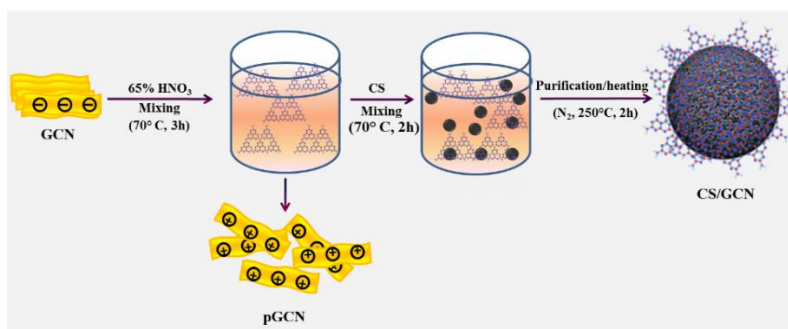


Figure 11. Schematic illustrations of graphitic carbon nitride with carbon sphere (CS/GCN) hybrid preparation process.

3.2. Photocatalytic Tests

Acid Red 18 (AR18) was selected as a model dye to evaluate the photoactivity of the synthesized samples under simulated solar light irradiation (150 W xenon lamp with cut-off light filters of natural solar condition, Air Mass 1.5G). Typically, in a photocatalytic experiment, 30 mg of photocatalyst was dispersed in 100 mL of AR18 aqueous solution (10 mg/dm³) and placed in a quartz glass reactor. In order to avoid evaporation of reaction solution, water cooling of reactor was applied. Before irradiation the suspension was stirred in the darkness for 1 h to achieve the adsorption–desorption equilibrium. Afterwards, the mixture was irradiated for 48 h. At regular intervals, about 2 mL of the reaction mixture was taken from the suspension and the absorbance was measured by UV-vis spectrophotometer (Helios alpha, Thermo Fisher Scientific, Waltham, MA, USA). The degree of AR18 decomposition was calculated according to the equation C/C_0 where C_0 is the initial concentration of the dye solution and C is the concentration at time t .

3.3. Characterization

The morphology and structure of the obtained materials was analyzed by transmission electron microscopy using an FEI Tecnai G2 F20 S Twin with an accelerating voltage of 200 kV (Frequency Electronics Inc., Thermo Fisher Scientific, Waltham, MA, USA) and scanning electron microscopy (TESCAN, VEGA SBU3), acquired at 30 kV acceleration voltage. The atomic force microscope (AFM) study was carried out using atomic force microscope (Nanoscope V Multimode 8, Bruker AXS, Mannheim, Germany). Powder X-ray diffraction (XRD) patterns were recorded using an X'Pert Philips PRO X-ray diffractometer employing CuK α radiation (X'Pert PRO Philips diffractometer, Almelo, The Netherlands). The optical properties of the produced materials were investigated by diffuse reflectance (DR) UV-vis technique using a Jasco spectrometer (Tokyo, Japan). Raman spectra were recorded via Renishaw In Via Raman spectroscope with excitation wavelength of 785 nm (New Mills, Kingswood, Wotton-under-Edge, UK). The room temperature photoluminescence spectroscopy (PL) measurements at 650 nm excitations were performed using fluorescence spectrophotometer F7000 (Hitachi). The specific surface area of nanomaterials was calculated by the Brunauer–Emmett–Teller

(BET) method using Micromeritics ASAP 2010M apparatus (Norcross, USA). The potential value of water-based suspension of the samples was revealed in Zeta potential measurements performed via Zeta Sizer (ZS NanoMalvern Panalytical, Malvern, UK). Electrochemical impedance spectroscopy was investigated using BioLogic VMP-3 potentiostat (Bio-Logic Science Instruments, Seyssinet-Pariset, France) station with a standard three-electrode system. A saturated calomel electrode Hg|Hg₂Cl₂, KCl(sat.) (SCE) was used as a reference electrode and a platinum wire (surface area ~5 cm²) as a counter electrode. To prepare the working electrode (WE, 5 mm diameter glassy carbon disk in PEEK polymer case, ALS Co., Ltd., Japan), 2 mg of catalyst was sonicated in isopropanol, loaded onto WE surface (5 µL) and dried for 12 h. The electrochemical measurement was examined in water solution of redox salts K₃[Fe(CN)₆]/K₄[Fe(CN)₆], 2.5 mM/2.5 mM with 0.5 M sodium sulfate as base electrolyte.

Linear Sweep Potentiometry (LSV) and Photocurrent response measurements (Chronoamperometry) were recorded by Autolab PGSTAT302N potentiostat (Herisau, Switzerland) in a three-electrode test cell with a platinum wire as counter electrode and saturated calomel electrode as reference. A 60 W LED with 400–700 nm filter was used as a light source. A total of 2 mg of catalyst was sonicated in ethanol–water solution (volume ratio 1:3) and 25 µL of Nafion solution (5 wt%) for 15 min. 50 µL of obtained homogenous solution was drop-casted onto FTO (Fluorine-doped Tin Oxide) glass slide (Sigma Aldrich). As-prepared working electrode was placed inside the test cell. 0.5 M sodium sulfate was used as the electrolyte in all electrochemical measurements. LSV test was performed from 0.15 V to 1.4 V versus SCE with 50 mV/s scan rate. Photocurrent test was measured at 0.5 V versus SCE.

4. Conclusions

In summary, the spherical core/shell hybrid based on ordered mesoporous carbon and graphitic carbon nitride was prepared via simple and reproducible approach. The as-synthesized non-metal hybrid exhibited superior photocatalytic activity toward organic dye decomposition under vis-light irradiation. The synergistic effect caused by above-mentioned components heterojunction improved carbon nitride properties and successfully eliminated the major drawbacks which hindered its industrial application. The photocatalytic performance of CS/GCN was nine times higher in comparison to the bulk GCN. The catalyst also showed high stability after three recycles. The electrochemical tests enabled confirmation that charge carrier generation and retardation of the electron–hole recombination were significantly enhanced. The results allowed us to understand how mesoporous carbon spheres influenced the photocatalytic activity of graphitic carbon nitride. Basing on detailed characterization of the materials, we found that coupling g-C₃N₄ with mesoporous carbon affected modification in the band alignment of the hybrid, which had an effect on the mechanism of reactive oxidative species formation that was involved in the photodegradation process. This study presents the preparation route for anew superb metal-free hybrid, which can be suitable for the dye wastewater treatment under visible light.

Supplementary Materials: The following are available online at <http://www.mdpi.com/2073-4344/9/12/1007/s1>, Figure S1: The photocatalytic degradation of melamine over CS/GCN under simulated solar light irradiation.

Author Contributions: Conceptualization, R.J.K. and B.Z.; Funding acquisition, R.J.K. and M.A.; Investigation, M.B., M.A. and B.Z.; Writing-Original Draft Preparation, B.Z., M.B. and M.A.; Writing-Review & Editing, B.Z., M.B. and M.A.; Supervision, R.J.K. and E.M.

Funding: This work was funded by National Science Centre, Poland (grant number 2016/21/B/ST8/02733 and 2015/19/D/ST5/01920).

Conflicts of Interest: The authors declare no conflict of interest.

References

1. Zhao, Z.; Sun, Y. Dong. *Graphitic carbon nitride based nanocomposites: a review*. *Nanoscale* **2015**, *7*, 15–37. [PubMed]
2. Capilli, G.; Costamagna, M.; Sordello, F.; Minero, C. Synthesis, characterization and photocatalytic performance of p-type carbon nitride. *Appl. Catal. B* **2019**, *242*, 121–131. [CrossRef]

3. Wang, Y.; Zhao, X.; Cao, D.; Wang, Y.; Zhu, Y. Peroxymonosulfate enhanced visible light photocatalytic degradation bisphenol A by single-atom dispersed Ag mesoporous g-C₃N₄ hybrid. *Appl. Catal. B* **2017**, *211*, 79–88. [[CrossRef](#)]
4. Zhu, B.; Zhang, J.; Jiang, C.; Cheng, B.; Yu, J. First principle investigation of halogen-doped monolayer g-C₃N₄ photocatalyst. *Appl. Catal. B* **2017**, *207*, 27–34. [[CrossRef](#)]
5. Hao, R.; Wang, G.; Tang, H.; Sun, L.; Xu, C.; Han, D. Template-free preparation of macro/mesoporous g-C₃N₄/TiO₂ heterojunction photocatalysts with enhanced visible light photocatalytic activity. *Appl. Catal. B* **2016**, *187*, 47–58. [[CrossRef](#)]
6. Wen, J.; Xie, J.; Chen, X.; Li, X. A review on g-C₃N₄-based photocatalysts. *Appl. Surf. Sci.* **2017**, *391*, 72–123. [[CrossRef](#)]
7. Chen, D.; Wang, K.; Hong, W.; Zong, R.; Yao, W.; Zhu, Y. Visible light photoactivity enhancement via CuTCPP hybridized g-C₃N₄ nanocomposite. *Appl. Catal. B* **2015**, *166–167*, 366–373. [[CrossRef](#)]
8. Mamba, G.; Mishra, A.K. Graphitic carbon nitride (g-C₃N₄) nanocomposites: A new and exciting generation of visible light driven photocatalysts for environmental pollution remediation. *Appl. Catal. B* **2016**, *198*, 347–377. [[CrossRef](#)]
9. Jiang, L.; Yuan, X.; Pan, Y.; Liang, J.; Zeng, G.; Wu, Z.; Wang, H. Doping of graphitic carbon nitride for photocatalysis: A review. *Appl. Catal. B* **2017**, *217*, 388–406. [[CrossRef](#)]
10. Jun, Y.S.; Hong, W.H.; Antonietti, M.; Thomas, A. Mesoporous, 2D Hexagonal Carbon Nitride and Titanium Nitride/Carbon Composites. *Adv. Mater.* **2009**, *21*, 4270–4274. [[CrossRef](#)]
11. Yang, S.B.; Feng, X.L.; Wang, X.C.; Mullen, K. Graphene-Based Carbon Nitride Nanosheets as Efficient Metal-Free Electrocatalysts for Oxygen Reduction Reactions. *Angew. Chem. Int. Ed.* **2011**, *50*, 5339–5343. [[CrossRef](#)] [[PubMed](#)]
12. Wang, J.; Yang, Z.; Gao, X.; Yao, W.; Wei, W.; Chen, X.; Zong, R.; Zhu, Y. Core-shell g-C₃N₄@ZnO composites as photoanodes with double synergistic effects for enhanced visible-light photoelectrocatalytic activities. *Appl. Catal. B* **2017**, *217*, 169–180. [[CrossRef](#)]
13. Karimi, L. Combination of mesoporous titanium dioxide with MoS₂ nanosheets for high photocatalytic activity. *Pol. J. Chem. Technol.* **2017**, *19*, 56–60. [[CrossRef](#)]
14. Xu, M.; Han, L.; Dong, S. Facile Fabrication of Highly Efficient g-C₃N₄/Ag₂O Heterostructured Photocatalysts with Enhanced Visible-Light Photocatalytic Activity. *ACS Appl. Mater. Interf.* **2013**, *5*, 12533–12540. [[CrossRef](#)]
15. Xu, H.; Yan, J.; Xu, Y.; Song, Y.; Li, H.; Xia, J.; Huang, C.; Wan, H. Novel visible-light-driven AgX/graphite-like C₃N₄ (X = Br, I) hybrid materials with synergistic photocatalytic activity. *Appl. Catal. B* **2013**, *129*, 182–193. [[CrossRef](#)]
16. Kumar, T.; Surendar, A.; Baruah, V.; Shanker, J. Synthesis of a novel and stable g-C₃N₄-Ag₃PO₄ hybrid nanocomposite photocatalyst and study of the photocatalytic activity under visible light irradiation. *Mater. Chem. A* **2013**, *1*, 5333–5340. [[CrossRef](#)]
17. Jiang, D.; Chen, L.; Zhu, J.; Chen, M.; Shi, W.; Xie, J. Novel p–n heterojunction photocatalyst constructed by porous graphite-like C₃N₄ and nanostructured BiOI: facile synthesis and enhanced photocatalytic activity. *Dalton Trans.* **2013**, *42*, 15726–15734. [[CrossRef](#)]
18. Ge, L.; Han, C.; Xiao, X.; Guo, L. Synthesis and characterization of composite visible light active photocatalysts MoS₂-g-C₃N₄ with enhanced hydrogen evolution activity. *Int. J. Hydrogen Energy* **2013**, *38*, 6960–6969. [[CrossRef](#)]
19. Cao, S.W.; Yuan, Y.P.; Fang, J.; Shahjamali, M.M.; Boey, F.Y.; Barber, J.; Loo, S.C.; Xue, C. In-situ growth of CdS quantum dots on g-C₃N₄ nanosheets for highly efficient photocatalytic hydrogen generation under visible light irradiation. *Int. J. Hydrogen Energy* **2013**, *38*, 1258–1266. [[CrossRef](#)]
20. Xu, H.; Song, Y.; Song, Y.; Zhu, J.; Zhu, T.; Liu, C.; Zhao, D.; Zhang, Q.; Li, H. Synthesis and characterization of g-C₃N₄/Ag₂CO₃ with enhanced visible-light photocatalytic activity for the degradation of organic pollutants. *RSC Adv.* **2014**, *4*, 34539–34547. [[CrossRef](#)]
21. Mousavi, M.; Habibi-Yangjeh, A. Magnetically separable ternary g-C₃N₄/Fe₃O₄/BiOI nanocomposites: Novel visible-light-driven photocatalysts based on graphitic carbon nitride. *J. Colloid Interface Sci.* **2016**, *465*, 83–92. [[CrossRef](#)] [[PubMed](#)]
22. Kumar, S.; Baruah, A.; Tonda, S.; Kumar, B.; Shanker, V.; Sreedhar, B. Cost-effective and eco-friendly synthesis of novel and stable N-doped ZnO/g-C₃N₄ core-shell nanoplates with excellent visible-light responsive photocatalysis. *Nanoscale* **2014**, *6*, 4830–4842. [[CrossRef](#)] [[PubMed](#)]

23. Zhang, Z.; Wang, M.; Cui, W.; Sui, H. Synthesis and characterization of a core-shell BiVO₄@g-C₃N₄ photo-catalyst with enhanced photocatalytic activity under visible light irradiation. *RSC Adv.* **2017**, *7*, 8167–8177. [[CrossRef](#)]
24. Shen, H.; Zhao, X.; Duan, L.; Liu, R.; Li, H. Enhanced visible light photocatalytic activity in SnO₂@g-C₃N₄ core-shell structures. *Mater. Sci. Eng. B* **2017**, *218*, 23–30. [[CrossRef](#)]
25. Lu, D.; Wang, H.; Zhao, X.; Kondamareddy, K.K.; Ding, J.; Li, C.; Fang, P. Highly Efficient Visible-Light-Induced Photoactivity of Z-Scheme g-C₃N₄/Ag/MoS₂ Ternary Photocatalysts for Organic Pollutant Degradation and Production of Hydrogen. *ACS Sustain. Chem. Eng.* **2017**, *5*, 1436–1445. [[CrossRef](#)]
26. Ma, L.; Wang, G.; Jiang, C.; Bao, H.; Xu, Q. Synthesis of core-shell TiO₂@g-C₃N₄ hollow microspheres for efficient photocatalytic degradation of rhodamine B under visible light. *Appl. Surf. Sci.* **2017**, *430*, 263–272. [[CrossRef](#)]
27. Yao, Y.; Lu, F.; Zhu, Y.; Wei, F.; Liu, X.; Lian, C.; Wang, S. Magnetic core-shell CuFe₂O₄@C₃N₄ hybrids for visible light photocatalysis of Orange II. *J. Hazard. Mater.* **2015**, *297*, 224–233. [[CrossRef](#)]
28. Liu, S.; Ke, J.; Sun, H.; Liu, J.; Tade, M.O.; Wang, S. Size dependence of uniform carbon spheres in promoting graphitic carbon nitride toward enhanced photocatalysis. *Appl. Catal. B* **2017**, *204*, 358–364. [[CrossRef](#)]
29. Li, K.; Xie, X.; Zhang, W.D. Photocatalysts based on g-C₃N₄-encapsulating carbon spheres with high visible light activity for photocatalytic hydrogen evolution. *Carbon* **2016**, *110*, 356–366. [[CrossRef](#)]
30. Papailias, I.; Todorova, N.; Giannakopoulou, T.; Ioannidis, N.; Boukosa, N.; Athanasekou, C.P.; Dimotikali, D.; Trapalis, C. Chemical vs thermal exfoliation of g-C₃N₄ for NO_x removal under visible light irradiation. *Appl. Catal. B* **2018**, *239*, 16–26. [[CrossRef](#)]
31. Cao, S.; Low, J.; Yu, J.; Jaroniec, M. Polymeric photocatalysts based on graphitic carbon nitride. *Adv. Mater.* **2015**, *27*, 2150–2176. [[CrossRef](#)] [[PubMed](#)]
32. Zheng, Y.; Lin, L.; Wang, B.; Wang, X. Graphitic carbon nitride polymers toward sustainable photoredox catalysis. *Angew. Chem. Int. Ed.* **2015**, *54*, 12868–12884. [[CrossRef](#)] [[PubMed](#)]
33. Ma, L.; Fan, H.; Fu, K.; Lei, S.; Hu, Q. Protonation of Graphitic Carbon Nitride (g-C₃N₄) for an Electrostatically Self-Assembling Carbon@g-C₃N₄ Core-Shell Nanostructure toward High Hydrogen Evolution. *ACS Sustain. Chem. Eng.* **2017**, *5*, 7093–7103. [[CrossRef](#)]
34. Ong, W.-J.; Tan, L.-L.; Chai, S.-P.; Yong, S.-T.; Mohamed, A.R. Surface charge modification via protonation of graphitic carbon nitride (g-C₃N₄) for electrostatic self-assembly construction of 2D/2D reduced graphene oxide (rGO)/g-C₃N₄ nanostructures toward enhanced photocatalytic reduction of carbon dioxide to methane. *NanoEnergy* **2015**, *13*, 757–770. [[CrossRef](#)]
35. Zhang, Y.; Shao, D.; Yan, J.; Jia, X.; Li, Y.; Yu, P.; Zhang, T.J. The pore size distribution and its relationship with shale gas capacity in organic-rich mudstone of Wufeng-Longmaxi Formations, Sichuan Basin, China. *Nat. Gas Geosci.* **2016**, *1*, 213–220. [[CrossRef](#)]
36. Sing, K.S.W.; Williams, R.T. Physisorption Hysteresis Loops and the Characterization of Nanoporous Materials. *Adsorpt. Sci. Technol.* **2004**, *22*, 773–782. [[CrossRef](#)]
37. Thommes, M.; Kaneko, K.; Neimark, A.V.; Olivier, J.P.; Rodriguez-Reinoso, F.; Rouquerol, J.; Sing, K.S.W. Physisorption of gases, with special reference to the evaluation of surface area and pore size distribution (IUPAC Technical Report). *Pure Appl. Chem.* **2015**, *87*, 1051–1069. [[CrossRef](#)]
38. Li, T.; Jiang, Z.; Xu, C.; Liu, B.; Liu, G.; Wang, P.; Li, X.; Chen, W.; Ning, C.; Wang, Z. Effect of pore structure on shale oil accumulation in the lower third member of the Shahejie formation, Zhanhua Sag, eastern China: Evidence from gas adsorption and nuclear magnetic resonance. *Mar. Pet. Geol.* **2017**, *88*, 932–949. [[CrossRef](#)]
39. Wang, P.; Jiang, Z.; Chen, L.; Yin, L.; Li, Z.; Zhang, C.; Tang, X.; Wang, G. Pore structure characterization for the Longmaxi and Niutitang shales in the Upper Yangtze Platform, South China: Evidence from focused ion beam-He ion microscopy, nano-computerized tomography and gas adsorption analysis. *Mar. Pet. Geol.* **2018**, *77*, 1323–1337. [[CrossRef](#)]
40. Bommier, C.; Luo, W.; Gao, W.-Y.; Greaney, A.; Ma, S.; Ji, X. Predicting capacity of hard carbon anodes in sodium-ion batteries using porosity measurements. *Carbon* **2014**, *76*, 165–174. [[CrossRef](#)]
41. Mohini, R.; Lakshminarasimhan, N. Coupled semiconductor nanocomposite g-C₃N₄/TiO₂ with enhanced visible light photocatalytic activity. *Mater. Res. Bull.* **2016**, *76*, 370–375. [[CrossRef](#)]
42. Guo, X.; Wang, Y.; Wu, F.; Ni, Y.; Kokot, S. Preparation of protonated, two-dimensional graphitic carbon nitride nanosheets by exfoliation, and their application as a fluorescent probe for trace analysis of copper(II). *Microchim. Acta* **2016**, *183*, 773–780. [[CrossRef](#)]

43. Pawar, R.C.; Kang, S.; Park, J.H.; Kim, J.H.; Ahn, S.; Lee, C.S. Room-temperature synthesis of nanoporous 1D microrods of graphitic carbon nitride ($g\text{-C}_3\text{N}_4$) with highly enhanced photocatalytic activity and stability. *Sci. Rep.* **2016**, *6*, 31147. [[CrossRef](#)] [[PubMed](#)]
44. Zhang, M.; Bai, X.; Liu, D.; Wang, J.; Zhu, Y. Enhanced catalytic activity of potassium-doped graphitic carbon nitride induced by lower valence position. *Appl. Catal. B* **2015**, *164*, 77–81. [[CrossRef](#)]
45. Wang, Y.Y.; Yang, W.J.; Chen, X.J.; Wang, J.; Zhu, Y.F. Photocatalytic activity enhancement of core-shell structure $g\text{-C}_3\text{N}_4/\text{TiO}_2$ via controlled ultrathin $g\text{-C}_3\text{N}_4$ layer. *Appl. Catal. B* **2018**, *220*, 337–347. [[CrossRef](#)]
46. Tonda, S.; Kumar, S.; Kandula, S.; Shanker, V.J. Fe-doped and -mediated graphitic carbon nitride nanosheets for enhanced photocatalytic performance under natural sunlight. *J. Mater. Chem. A* **2014**, *2*, 6772–6780. [[CrossRef](#)]
47. Hu, S.W.; Yang, L.W.; Tian, Y.; Wei, X.L.; Ding, J.W.; Zhong, J.X.; Chu, P.K. Simultaneous nanostructure and heterojunction engineering of graphitic carbon nitride via in situ Ag doping for enhanced photoelectrochemical activity. *Appl. Catal. B* **2015**, *163*, 611–622. [[CrossRef](#)]
48. Giannakopoulou, T.; Papailias, I.; Todorova, N.; Boukos, N.; Liu, Y.; Yu, J.G.; Trapalis, C.J. Tailoring the energy band gap and edges' potentials of $g\text{-C}_3\text{N}_4/\text{TiO}_2$ composite photocatalysts for NO_x removal. *Chem. Eng.* **2017**, *310*, 571–580. [[CrossRef](#)]
49. Zinin, P.V.; Ming, L.C.; Sharma, S.K.; Khabashesku, V.N.; Liu, X.; Hong, S.; Endo, S.; Acosta, T. Ultraviolet and near-infrared Raman spectroscopy of graphitic C_3N_4 phase. *Chem. Phys. Lett.* **2009**, *472*, 69–73. [[CrossRef](#)]
50. Jin, Y.Z.; Gao, C.; Hsu, W.K.; Zhu, Y.; Huczko, A.; Bystrzejewski, M.; Roe, M.; Lee, C.Y.; Acquah, S.; Kroto, H.; et al. Large-scale synthesis and characterization of carbon spheres prepared by direct pyrolysis of hydrocarbons. *Carbon* **2005**, *43*, 1944–1953. [[CrossRef](#)]
51. Wang, Y.; Wang, X.; Antonietti, M. Polymeric Graphitic Carbon Nitride as a Heterogeneous Organocatalyst: From Photochemistry to Multipurpose Catalysis to Sustainable Chemistry. *Angew. Chem. Int. Ed.* **2012**, *51*, 68–89. [[CrossRef](#)] [[PubMed](#)]
52. Zhang, X.; Cao, S.; Wu, Z.; Zhao, S.; Piao, L. Enhanced photocatalytic activity towards degradation and H_2 evolution over one dimensional $\text{TiO}_2/\text{MWCNTs}$ heterojunction. *Appl. Surf. Sci.* **2017**, *402*, 360–368. [[CrossRef](#)]
53. Wang, H.; Yuan, X.Z.; Wu, Y.; Zeng, G.M.; Chen, X.H.; Leng, L.J.; Li, H. Synthesis and applications of novel graphitic carbon nitride/metal-organic frameworks mesoporous photocatalyst for dyes removal. *Appl. Catal. B* **2015**, *174*, 445–454. [[CrossRef](#)]
54. Ye, S.; Qiu, L.-G.; Yuan, Y.-P.; Zhu, Y.-J.; Xia, J.; Zhu, J.-F. Facile fabrication of magnetically separable graphitic carbon nitride photocatalysts with enhanced photocatalytic activity under visible light. *J. Mater. Chem. A* **2013**, *1*, 3008–3015. [[CrossRef](#)]
55. Cinelli, G.; Cuomo, F.; Ambrosone, L.; Colella, M.; Ceglie, A.; Venditti, F.; Lopez, F.J. Photocatalytic degradation of a model textile dye using carbon-doped titanium dioxide and visible light. *Water Process Eng.* **2017**, *20*, 71–77. [[CrossRef](#)]
56. Venditti, F.; Cuomo, F.; Ceglie, A.; Avino, P.; Russo, M.V.; Lopez, F. Visible Light caffeic acid degradation by carbon-doped titanium dioxide. *Langmuir* **2015**, *31*, 3627–3634. [[CrossRef](#)]
57. Sin, J.C.; Lam, S.M.; Lee, K.T.; Mohamed, A.R. Preparation and photocatalytic properties of visible light-driven samarium-doped ZnO nanorods. *Ceram. Int.* **2013**, *39*, 5833–5843. [[CrossRef](#)]
58. Raza, W.; Haque, M.M.; Muneer, M.; Fleisch, M.; Hakki, A.; Bahnemann, D.J. Photocatalytic degradation of different chromophoric dyes in aqueous phase using La and Mo doped TiO_2 hybrid carbon spheres. *Alloys Compd.* **2015**, *632*, 837–844. [[CrossRef](#)]
59. Wu, F.; Li, X.; Liu, W.; Zhang, S. Highly enhanced photocatalytic degradation of methylene blue over the indirect all-solid-state Z-scheme $g\text{-C}_3\text{N}_4\text{-RGO-TiO}_2$ nanoheterojunctions. *Appl. Surf. Sci.* **2017**, *405*, 60–70. [[CrossRef](#)]
60. Chen, F.; Yang, Q.; Wang, S.; Yao, F.; Sun, J.; Wang, Y.; Zhang, C.; Li, X.; Niu, C.; Wang, D.; et al. Graphene oxide and carbon nitride nanosheets co-modified silver chromate nanoparticles with enhanced visible-light photoactivity and anti-photocorrosion properties towards multiple refractory pollutants degradation. *Appl. Catal. B* **2017**, *209*, 493–505. [[CrossRef](#)]
61. Liu, T.; Wang, L.; Lu, X.; Fan, J.; Cai, X.; Gao, B.; Miao, R.; Wang, J.; Lv, Y. Comparative study of the photocatalytic performance for the degradation of different dyes by ZnIn_2S_4 : adsorption, active species, and pathways. *RSC Adv.* **2017**, *7*, 12292–12300. [[CrossRef](#)]

62. Konstantinou, K.I.; Albanis, T.A. TiO₂-assisted photocatalytic degradation of azo dyes in aqueous solution: kinetic and mechanistic investigations: A review. *Appl. Catal. B* **2004**, *49*, 1–14. [[CrossRef](#)]
63. Rajeshwar, K.; Osugi, M.E.; Chanmanee, W.; Chenthamarakshan, C.R.; Zaroni, M.V.B.; Kajitichyanukul, P.; Krishnan-Ayer, R. Heterogeneous photocatalytic treatment of organic dyes in air and aqueous media. *J.Photochem. Photobiol. C* **2008**, *9*, 171–192. [[CrossRef](#)]



© 2019 by the authors. Licensee MDPI, Basel, Switzerland. This article is an open access article distributed under the terms and conditions of the Creative Commons Attribution (CC BY) license (<http://creativecommons.org/licenses/by/4.0/>).